Lab on a Chip

PAPER

View Article Online
View Journal | View Issue

Cite this: *Lab Chip*, 2015, **15**, 3021

Flow-through microfluidic photoionization detectors for rapid and highly sensitive vapor detection†

Hongbo Zhu,[a] Robert Nidetz,[b] Menglian Zhou,[a] Jiwon Lee,[a] Sanketh Buggaveeti,[b] Katsuo Kurabayashi[b] and Xudong Fan*[a]

Received 17th March 2015,
Accepted 26th May 2015

DOI: 10.1039/c5lc00328h

www.rsc.org/loc

A photoionization detector (PID) is well known for its high sensitivity, large dynamic range, and non-destructive vapor detection capability. However, due to its tardy response, which results from the relatively large ionization chamber and dead volume, the application of the PID in gas chromatography (GC) has been limited. Here, we developed a rapid, flow-through, and highly sensitive microfluidic PID that was microfabricated directly on a conductive silicon wafer. The microfluidic PID has a significantly reduced ionization chamber volume of only 1.3 μL, nearly 10 times smaller than that of state-of-the-art PIDs and over 100 times smaller than that of commercial PIDs. Moreover, it has virtually zero dead volume due to its flow-through design. Consequently, the response time of the microfluidic PID can be considerably shortened, ultimately limited by its residence time (7.8 ms for 10 mL min^{-1} and 78 ms for 1 mL min^{-1}). Experimentally, the response of the microfluidic PID was measured to be the same as that of the standard flame ionization detector with peak full-widths-at-half-maximum of 0.25 s and 0.085 s for flow rates of 2.3 mL min^{-1} and 10 mL min^{-1}, respectively. Our studies further show that the microfluidic PID was able to detect analytes down to the picogram level (at 3σ of noise) and had a linear dynamic range of six orders of magnitude. Finally, because of the very short distance between the electrodes, low voltage (<10 VDC, over 10 times lower than that in a regular PID) can be used for microfluidic PID operation. This work will open a door to broad applications of PIDs in gas analyzers, in particular, micro-GC and multi-dimensional GC.

Introduction

Gas chromatography (GC) is widely used in analysis of volatile organic compounds (VOCs). Miniaturized versions of GC, *i.e.*, micro-GC (μGC) are under intensive development for possible field applications. One critical component inside a μGC device is the vapor detector, which must be lightweight, small in footprint, rapid, sensitive, and able to operate using low power/voltage. In addition, non-destructive and flow-through characteristics are highly desirable for consecutive vapor analysis in multi-dimensional μGC without destroying analytes or GC elution profiles.[1]

Flame ionization detectors (FIDs) are commonly used vapor detectors in bench-top GC instruments. They have high sensitivity (picogram), large dynamic range (6 orders of magnitude), and zero dead volume. Miniaturized FIDs (μFIDs) are being developed for portable applications.[2–6] However, FIDs and μFIDs are destructive and cannot be placed in the middle of the vapor flow path to monitor multi-dimensional GC separation. Instead, they are used only at the terminal end of a GC instrument. Furthermore, the required use of hydrogen hinders their broad acceptance in μGC devices. Thermal conductivity detectors (TCDs) and μTCDs have also been used as vapor detectors.[7,8] They are non-destructive and have a flow-through design. However, TCDs suffer from low sensitivity (nanogram) and require helium. Electron capture detectors (ECDs) are another type of non-destructive vapor detector.[7] While they are very sensitive, they have a limited dynamic range and need to use radioactive materials for analyte ionization. Recently, many other types of miniaturized non-destructive vapor detectors have been developed for μGC applications, including surface acoustic waves (SAWs),[9–11] chemicapacitors,[12,13] chemiresistors,[9,14] optical vapor sensors,[15–22] and nanoelectronic sensors.[23,24] These sensors are small in footprint and non-destructive. However, they may suffer from either large dead volumes,[9–14] low sensitivity,[9,12–14] electrical–optical–electrical conversions (for all optical vapor sensors) or limited vapor types.[23,24] In addition, these vapor sensors usually require polymer coatings on

[a] *Department of Biomedical Engineering, University of Michigan, 1101 Beal Avenue, Ann Arbor, Michigan 48109, USA. E-mail: xsfan@umich.edu*
[b] *Department of Mechanical Engineering, University of Michigan, 2350 Hayward, Ann Arbor, Michigan, 48109, USA*

† Electronic supplementary information (ESI) available. See DOI: 10.1039/c5lc00328h

their surface to capture analytes, which may slow down the detection speed due to the adsorption and desorption processes.

The photoionization detector (PID) is another type of vapor detector that has been under development for the past 50 years.[25–34] They are sensitive (picogram), non-destructive, and applicable to a wide range of vapors. Furthermore, they have a large dynamic range (six orders of magnitude). Nevertheless, due to its tardy response resulting from the large ionization chamber and dead volume, the application of the PID in GC systems has been limited. A typical commercial PID has an ionization chamber volume of 40–200 μL with the dead volume being 1/4–1/6 of the chamber volume.[29] The corresponding response time is on the order of a few seconds. However, the sharp peaks are generated at an extremely high flow rate (30 mL min^{-1}) or by using make-up gas (20 mL min^{-1}) flow rates,[32,35–37] neither of which is desirable for a GC or μGC system due to complicated fluidic design and/or significant reduction in sensitivity. Recently, an improvement in the chamber design was made to reduce the chamber volume down to 10 μL. A 30 ms response time (defined as the time from the bottom to 90% of the peak height) or an FWHM (full-width-at-half-maximum) of 45 ms was achieved with a flow rate of 30 mL min^{-1}.[32] However, the response speed is still limited by the relatively large chamber (and the dead volume as well), which becomes problematic at low flow rates typically used in μGC. For example, the chamber volume alone can lead to a peak broadening of 600 ms for a flow rate of 1 mL min^{-1}, not to mention the additional broadening from the associated dead volume, for which the effective flow rate would be much lower. In order to achieve rapid response, a small ionization chamber volume and a small dead volume are needed. Unfortunately, a small chamber always comes at the expense of the size of the electrode (corresponding to ion collection efficiency) and UV illumination cross-section (corresponding to ionization efficiency), which reduces the sensitivity of the PID. Very recently, a micro-helium discharge PID was also developed by Agah's group, which utilizes high energy plasma (~20 eV) generated by helium discharge to ionize an analyte.[33,34] The initial results indicated a detection limit of 350 pg.[33] The latest work reported during the review of this article showed impressive improvement as the micro-discharge PID was integrated into a micro-fabricated GC with a detection limit as low as approximately 10 pg.[34] The drawbacks of this type of PID include the need for helium and high voltage (>500 V) for plasma generation.

In this work, we developed a rapid, flow-through, and highly sensitive microfluidic PID that is micro-fabricated directly on a conductive silicon wafer with an Archimedean spiral channel commonly used in μGC columns[38,39] and can be operated with low voltage (<10 VDC, over 10 times lower than that used in a regular PID[27,32,40]). The microfluidic PID has a significantly reduced ionization chamber volume of only 1.3 μL, nearly 10 times smaller than that of state-of-the-art PIDs and over 100 times smaller than commercial PIDs. Moreover, it has virtually zero dead volume (~2 nL) due to its flow-through design. Consequently, the response time of the microfluidic PID can be considerably shortened, ultimately limited by its residence time (7.8 ms for 10 mL min^{-1} and 78 ms for 1 mL min^{-1}). Experimentally, the PID response is found to be the same as that of the standard flame ionization detector (FID) with peak FWHMs of 0.25 s and 0.085 s for flow rates of 2.3 mL min^{-1} and 10 mL min^{-1}, respectively. Our studies further show that the microfluidic PID was able to detect analytes down to the picogram level (at 3 standard deviations) due to the large UV illumination area and electrode area. A linear dynamic range of six orders of magnitude was achieved due to more uniform and sufficient UV ionization. Finally, because of the very short distance between the electrodes, only 6 VDC was needed for microfluidic PID operation. A detailed comparison among the micro-PID,[32] micro-discharge PID,[34] and microfluidic PID (current work) is given in Table S1.†

Theoretical analysis

Response time

The response time of a PID, t_{PID}, which contributes to GC peak broadening, is mainly governed by its ionization chamber volume and dead volume, *i.e.*,

$$(t_{PID})^2 \approx (t_{residence})^2 + (t_{dead})^2 = \left(\frac{V_{flow}}{F}\right)^2 + \left(\frac{V_{dead}}{F'}\right)^2, \quad (1)$$

where $t_{residence}$ is the residence time for most of the analyte to flow through the PID chamber and t_{dead} represents the residual time that is needed for the analyte in the dead volume to be swept out of the PID. V_{flow} and V_{dead} are the chamber flow volume (*i.e.*, the volume in the chamber swept by the mobile phase) and dead volume (*i.e.*, the volume in the chamber not swept by the mobile phase), respectively. V_{flow} + V_{dead} = total chamber volume. F and F' are the volumetric flow rate of the analyte residing in the chamber flow volume and dead volume, respectively. For a non-flow-through PID design, the dead volume is usually 1/6–1/4 of the chamber volume[29] and is responsible for the tailing effect in GC peaks. While t_{dead} is difficult to estimate, $t_{residence}$ for various PID designs can easily be calculated, as presented in Table 1. The PID response time is ultimately limited by its chamber volume (assuming that the dead volume is zero). Fig. S1 and 2† plot the COMSOL simulation results for various chamber sizes and the corresponding fall time in PID response. It is clearly shown that a small chamber size and a good fluidic design can significantly improve the PID response time.

Sensitivity

The current signal generated by a PID, i, can be expressed as:[28,29]

$$i \propto C \cdot I_0 A \sigma_i [AB], \quad (2)$$

Table 1 Analyte residence time for commercial PID, state-of-the-art PID, and microfluidic PID

Chamber volume	Commercial PID (100 μL)	State-of-the-art PID (10 μL)	Microfluidic PID (1.3 μL)
$t_{residence}$ for 1 mL min^{-1}	6 s	0.6 s	0.078 s
$t_{residence}$ for 5 mL min^{-1}	1.2 s	0.12 s	0.016 s

where I_0 is the vacuum ultraviolet (VUV) photon flux (in units of number of photons per m^2 per second), A is the effective VUV radiation area of an ionization chamber, σ_i is the ionization cross-section, [AB] is the analyte concentration, and C is the ion/electron collection efficiency at the electrodes. For a given analyte concentration and VUV light source, I_0, σ_i, and [AB] are fixed; therefore, i is linearly proportional to the radiation area. Usually, the VUV light source has a relatively large output diameter (*e.g.*, 3.5 mm for the lamp used in this work). However, in order to decrease the chamber volume for faster response, the effective radiation area in the traditional PID design is significantly reduced, and therefore, the VUV lamp is significantly underutilized. In addition, in order to increase the ion collection efficiency, a relatively high voltage (a few hundreds of volts) is needed to reduce ion recombination and quenching that adversely impact the detection signal.[27,32,40]

In contrast, the microfluidic PID uses a serpentine channel that reduces the chamber volume and eliminates the dead volume while maintaining a large VUV illumination area. Furthermore, the ion collection efficiency is improved due to the significantly reduced distance between the two electrodes and increased electrode area. The short distance increases the electric field strength for a given applied voltage and reduces ion recombination and quenching.[28,29] Consequently, the microfluidic PID can be operated with only 6 VDC. In addition, due to the short VUV illumination path, the analyte at different depths can be ionized more uniformly to ensure detection linearity.

Experimental

Materials

Highly doped p-type <100> single-sided polished conductive Si wafers with a resistivity of 0.001–0.005 Ω cm and a thickness of 380 μm, and 500 μm thick Pyrex glass wafers were purchased from University Wafer Company (Boston, MA, P/N 1318 and P/N 1112, respectively). A 10.6 eV VUV Kr lamp with a MgF_2 crystal window was purchased from Baseline-Mocon (P/N 043-257). GC guard columns (250 μm i.d. and 380 μm o.d.) and HP-5 coated columns (250 μm i.d., 380 μm o.d. and 0.25 μm coating thickness) were purchased from Agilent. Optical adhesives (Norland® 81) were purchased from Norland (Cranbury, NJ). The commercial PID used in the experiments was acquired from Baseline-Mocon (P/N 043-234). The commercial flame ionization detector (FID) used in the experiments was pre-installed on a Varian 3800 GC instrument. Benzene (P/N 270709), toluene (P/N 650579), ethylbenzene (P/N 03080), *m*-xylene (P/N 95670), and hexane (P/N 34859) were purchased from Sigma-Aldrich (St. Louis, MO, USA) and used without further purification. The relevant properties of these VOCs are listed in Table 2.

Fabrication and assembly

The microfluidic PID consisting of an Archimedean spiral microchannel was fabricated on a conductive silicon wafer that was first anodically bonded to a Pyrex glass wafer (see Fig. 1(A)). Next, 2.0 μm of silicon dioxide was deposited on top of the silicon wafer using plasma-enhanced vapor deposition (PECVD) and patterned. After patterning a 2.0 μm thick aluminum layer using lithography, evaporation, and lift-off, deep reactive-ion etching (DRIE) was carried out to etch through the silicon wafer to form a final channel that had a cross-section of 150 μm (width) × 380 μm (depth), a wall thickness of 50 μm, and a length of 2.3 cm. The entire channel had an overall size of 15 mm × 15 mm (see Fig. 1(B) for part of the chip). In order to reduce the dead volume at the interconnection between the GC column and the microfluidic channel, the terminals of the microfluidic channel had a trapezoidal shape (400 μm (bottom width) × 150 μm (top width) × 100 μm (height)). The terminals of the microfluidic channel were further connected to an inlet/outlet port (5.9 mm in length) so that the guard columns could be inserted (Fig. 1(B) and (C)). The ionization chamber volume was 1.3 μL; the dead volume, which arises mainly from the connections between the GC column and the microfluidic PID inlet/outlet, was estimated to be ~2 nL.

After microfluidic channel fabrication, two electrodes were wire-bonded to the aluminum layer on the microchannel and connected to the voltage supply and the amplifier, respectively (Fig. 1(A) and (B)). Then, the VUV Kr lamp with a MgF_2 crystal window was mounted on the top of the microchannel and sealed with an optical adhesive. The lamp had an effective illumination diameter of 3.5 mm, and therefore, was able to cover the entire microfluidic PID area (2.4 mm × 2.4 mm). Finally, two 10 cm long guard columns were inserted into the

Table 2 Physical properties of the VOCs used in the experiment[41]

VOC	VP[a]	Density[b]	IP[c]
Benzene	75.1	876.50	9.25
Toluene	22.0	866.90	8.82
Ethylbenzene	7.15	866.50	8.76
m-Xylene	6.16	860.00	8.56
Hexane	121	654.80	10.18

[a] Vapor pressure (mm Hg) at 20 °C. [b] Mass density (kg m^{-3}). [c] Ionization potential (eV).

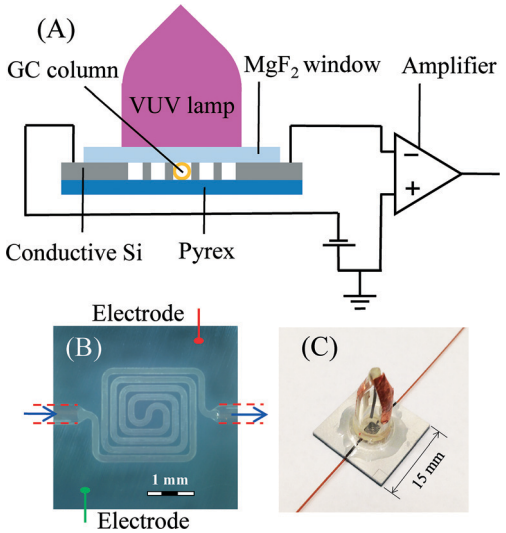

Fig. 1 (A) Overall microfluidic PID setup. The microfluidic gas channel (width: 150 μm, depth: 380 μm, wall thickness: 50 μm, total length: 2.3 cm) was formed on a conductive silicon wafer, which also provided two electrodes. The top part of the microfluidic channel was sealed with a MgF_2 window on which a VUV lamp (3.5 mm effective diameter) was placed to cover the entire microfluidic channel area (2.4 mm × 2.4 mm). The PID working principle is illustrated in Fig. S3.† (B) Microscopy image of the microfluidic channel portion of the PID. The corresponding electrode layout is shown in Fig. S4.† (C) Picture of the microfluidic PID with inlet/outlet columns and a VUV lamp attached.

inlet and outlet ports, respectively, and sealed with an optical adhesive.

Microfluidic PID operation

The details of microfluidic PID operation are illustrated in Fig. 1(A). In order to power the VUV lamp, we used the power drive circuit that came with the commercial PID (usually connected to a 5 VDC external voltage supply). The two electrodes on the microfluidic channel were connected to −6 VDC and ground, respectively, which generated an electric field of approximately 400 V cm^{-1} across the channel. The electrodes were further connected to an amplifier (Stanford Research Systems SR560, input impedance = 100 MΩ + 25 pF) to form a closed circuit. Based on the PID theory (see eqn (2)), the PID signal is directly generated from the charges of photoionized molecular fragments that produce current between the electrodes.[26,28,29] According to Ohm's law, the final voltage signal is proportional to the current signal across the internal resistance of the amplifier. During operation, the amplifier bandwidth was maintained at 10 Hz. The output voltage signal from the amplifier was acquired through a DAQ card (NI USB-6009, National Instruments, Austin, TX) *via* a LabView™ program. Note that although the p-type conductive silicon wafer has a high concentration of free holes, the photoelectric effect could still occur when the wafer was exposed to 10.6 eV VUV. As shown in Fig. S5,† when the VUV light was turned on, a baseline jump of approximately 94.3 mV with a noise of 0.68 mV (one standard deviation) was observed. Fig. S6† also displays the microfluidic PID temperature stability from 20 °C to 60 °C by placing the entire device inside a GC oven. When the temperature was below 40 °C, the baseline remained nearly the same as that for 20 °C. For the temperature close to the VUV lamp's specified maximal operating temperature (60 °C), a 44% increase in the baseline was observed, which is attributed to the increase in VUV lamp intensity, as evident in the 47% increase in the lamp drive current. However, the microfluidic PID noise remained constant (0.68 mV). In addition, the PID's sensitivity to the analyte stayed nearly unchanged (Fig. S6(B)†). The small (<10%) increase in the peak height was due to the narrower elution peak width at higher temperatures. In fact, detailed analysis shows that the peak area remained the same when the temperature varied from 20 °C to 60 °C, suggesting that the analyte was fully ionized due to the short (380 μm) UV illumination path (see more discussion in the "Detection limit" section). In the subsequent experiments, the microfluidic PID was operated at 20 °C unless otherwise specified. Therefore, the corresponding baseline was subtracted in data analysis.

Experimental setup

The overall experimental setup is shown in Fig. 2. We selected 5 analytes (benzene, toluene, ethylbenzene, *m*-xylene, and hexane) as model systems. The VOC samples and diluted gaseous samples were picked up at the headspace of the corresponding screw-thread vials and in Teflon septa-sealed vials, respectively, *via* a gas-tight syringe and then injected into the injection port of a Varian 3800 GC instrument with a split ratio of 60. For detector characterization, the detector (microfluidic PID, commercial PID, or FID) was connected to the GC injection port *via* a 3 m long guard column. For the

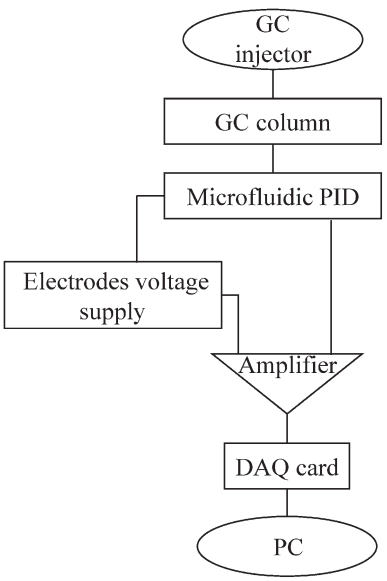

Fig. 2 Experimental setup.

VOC separation experiment, a 6 m long HP-5 column was used to replace the guard column. Helium was used as the carrier gas.

For comparison purposes, we also performed VOC measurement by using commercial PID and FID pre-installed on a Varian 3800 GC instrument to replace the microfluidic PID. To operate the commercial PID, we followed the instructions from the vendor. The GC column was connected to the inlet port of the commercial PID and the PID was driven by 5 VDC. The signals from the FID and the commercial PID were recorded directly by using the DAQ card without going through the SR560 amplifier.

Results and discussion

Response time

Compared with previously reported PIDs and commercial PIDs, which usually have a fluidic chamber volume in the range of tens to hundreds of μL (ref. 27, 29, and 32) and a dead volume of a few μL to tens of μL,[29] the microfluidic PID has a significantly reduced chamber volume of only 1.3 μL with a nearly negligible dead volume (~2 nL). The smaller chamber volume and dead volume translate directly to a faster detector response time.

Fig. 3(A) compares the flow rate dependent FWHM values of the microfluidic PID, commercial PID, and FID. As the flow rate increases from 2.3 mL min^{-1} to 10 mL min^{-1}, the microfluidic PID peak width (FWHM) decreases from 0.25 s to 0.085 s. The peak width is caused mainly by the dead volume in the GC injector and longitudinal dispersion of the analyte (toluene) in the GC column. In fact, Fig. 3(B) and (C) show that the microfluidic PID generates a peak width and shape virtually identical to that of the FID, which has zero dead volume. The fastest response time (defined as the time from the bottom to 90% of the peak height, approximately 65% of FWHM) for the microfluidic PID is about 0.055 s at a flow rate of 10 mL min^{-1}, close to 0.03 s obtained with the state-of-the-art PID at a flow rate of 30 mL min^{-1} and with a very short (0.2 m) column (no longitudinal dispersion). In contrast, the commercial PID, which has a chamber volume of ~200 μL, has a peak width of 1–2.5 s, consistent with the peak width achieved by other commercial PIDs under high flow rates.[32,35–37] Apparently, the peak width of the microfluidic PID is easily reduced by 10 folds compared to that of the commercial PID. Ultimately, the peak width is limited by the residence time determined by the PID chamber volume and dead volume. For the current microfluidic PID, the detection speed can be as fast as 78 ms for a flow rate of 1 mL min^{-1}, which can further be improved by using a shorter channel length or a smaller cross-section.

Detection limit

Fig. 4 plots the peak height as a function of injection mass for the five selected VOCs. While the peak height is similar for benzene, toluene, ethylbenzene, and *m*-xylene, it is much smaller for hexane, which is due to the high ionization

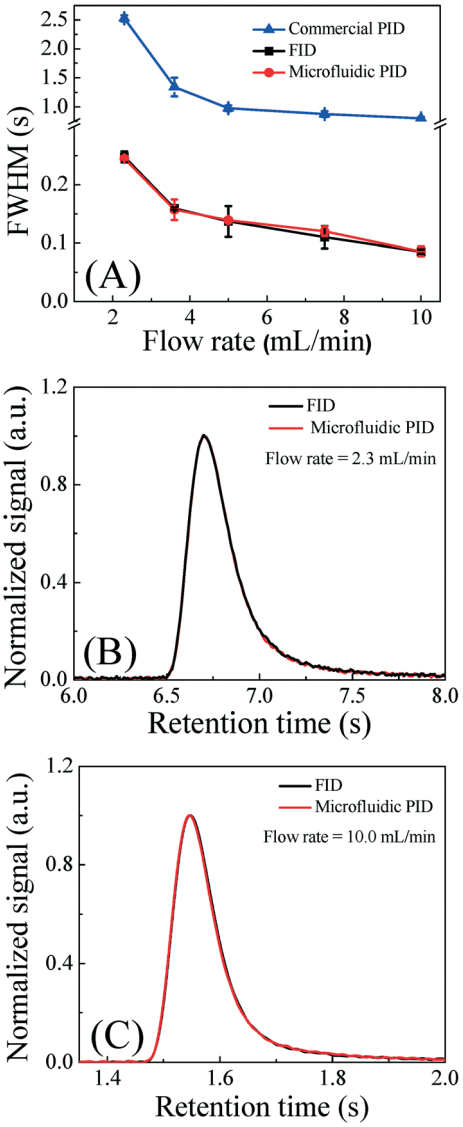

Fig. 3 (A) Comparison of full-width-at-half-maximum (FWHM) of the toluene peak obtained with commercial PID, FID, and microfluidic PID at various flow rates. Error bars are calculated based on four measurements. (B) and (C) Normalized toluene peak obtained with FID and microfluidic PID at flow rates of 2.3 mL min^{-1} and 10 mL min^{-1}, showing FWHMs of 0.25 s and 0.085 s, respectively. The response time measured from the bottom to 90% of the peak height is approximately 65% of the FWHM. The corresponding toluene peaks obtained with commercial PID are given in Fig. S7.†

potential (10.18 eV, close to 10.6 eV provided by the light of the VUV lamp). At low injection mass, the peak height increases linearly with respect to the injection mass with no change in the peak width, which is reflected in the unity slope of the curves on the log–log scale. At high injection masses (~1 μg), the peak height starts to saturate accompanied by peak broadening.

To estimate the detection limit, we considered the linearity of peak height *vs.* mass, signal-to-noise ratio, and a noise (σ) of 0.68 mV for the microfluidic PID. The corresponding detection limit equivalent to 3σ for the flow rate of 2.3 mL

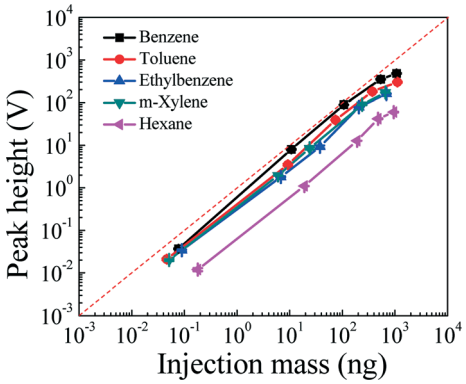

Fig. 4 Peak height obtained with the microfluidic PID as a function of injection mass for five different VOCs plotted on the log–log scale. The dashed line shows the curve with a unity slope to guide the eye. The detection limit (3σ) is 4.25 pg, 4.48 pg, 5.68 pg, 5.00 pg, and 30.6 pg for benzene, toluene, ethylbenzene, *m*-xylene, and hexane, respectively. The chromatographic peaks at the lowest injection mass are given in Fig. S8.†

min^{-1} is presented in Table 3. For comparison, Table 3 also lists the detection limit of the commercial PID and FID. It is found that the microfluidic PID can detect VOCs down to the single picogram level (except for hexane, which has an ionization potential close to the VUV photon energy). For the commercial PID, the detection limit is about 200 times higher than that for the microfluidic PID, which can partially be accounted for by the nearly 200 times larger chamber volume.

The excellent detection limit of the microfluidic PID is achieved by a combination of the large VUV illumination area, short illumination path, short electrode distance, and large electrode area. First, due to the serpentine structure of the microfluidic channel, the effective VUV illumination area is about 3.5 mm^2, about 60% of the entire area that the microfluidic channel occupies (2.4 mm × 2.4 mm, see Fig. 1(B)). In addition, due to the absorption of analytes, the VUV light intensity decays very rapidly when it passes through the ionization chamber. The short illumination path (380 μm) ensures that the analytes can be uniformly and efficiently ionized.

Second, during the photoionization process, recombination and quenching of anions and cations are enhanced with a longer transit time for ions to reach the electrodes. A simple calculation shows that the transit time is proportional to the distance of the electrodes and the inverse square root of the applied voltage (see eqn S1†). Therefore, decreasing the electrode distance is a more effective way of decreasing the transit time. The short distance between the electrodes (150 μm) in the microfluidic PID results in generation of a high electric field with only 6 VDC as well as suppression of recombination and quenching of ions, which, together with the large electrode area (8.74 mm^2), significantly enhances the ion collection efficiency and uniformity. The improved PID performance is reflected not only in the detection limit, but also in the linearity of the device responsivity curve, which will be discussed in the next section. A sub-linear responsivity curve indicates insufficient and non-uniform photoionization and ion collection.

Linearity

Besides the excellent sensitivity and detection limit, PIDs should exhibit a large linear detection range.[7,29] Fig. 5 presents the responsivity curves of the microfluidic PID for the five different VOCs with the injection mass ranging from below 50 pg to over 1000 ng. The peak areas in Fig. 5(A) show excellent linear response to the injection mass with an R^2 of 0.961–0.985 (see Table S2†) in the linear regression analysis (forced zero Y-intercept at zero injection mass). Due to the limitation of guard column capacity and sampling, the injection mass did not cover six orders of magnitude experimentally. Since the detection limit of the microfluidic PID is only a few picograms and, according to Fig. 4, at low injection masses, the peak area should decrease as the peak height decreases (but the peak width remains unchanged), we can infer that the linear range for the microfluidic PID spans six orders of magnitude from a few picograms to a few micrograms. In contrast, in ref. 32, although the injection mass (or concentration) is increased by six orders of magnitude, the sensing signal increases only about 1000 folds, indicating imperfect fluidic design as well as insufficient and non-uniform photoionization and ion collection. Finally, we note that the slope in Fig. 5 is given in V s per ng (see Table S2†). Except for hexane, which has an ionization potential very close to the VUV photon energy and is difficult to ionize, the remaining four VOCs have similar ionization potential, but their responsivity slope varies from 0.1 for benzene to 0.049 for ethylbenzene. However, the new slopes in units of V s per mol, achieved by multiplying each slope with the VOC's respective molecular weight, are close to each other (see Table S2†). This suggests that the microfluidic PID detects the molar concentration of the analyte, agreeing with the detection mechanism expected of a PID (see eqn (2)).

Table 3 Comparison of detection limit for FID, microfluidic PID, and commercial PID

	Benzene	Toluene	Ethylbenzene	*m*-Xylene	Hexane
FID	0.62 pg (0.2 ppt)	0.90 pg (0.24 ppt)	1.46 pg (0.34 ppt)	1.47 pg (0.34 ppt)	0.80 pg (0.23 ppt)
Microfluidic PID	4.25 pg (1.4 ppt)	4.48 pg (1.2 ppt)	5.68 pg (1.3 ppt)	5.00 pg (1.2 ppt)	30.6 pg (8.8 ppt)
Commercial PID	750 pg (240 ppt)	861 pg (230 ppt)	1354 pg (320 ppt)	1009 pg (230 ppt)	8081 pg (2300 ppt)

Part-per-trillion (ppt) is calculated for 1 L of gas at 1 atm and 300 K.

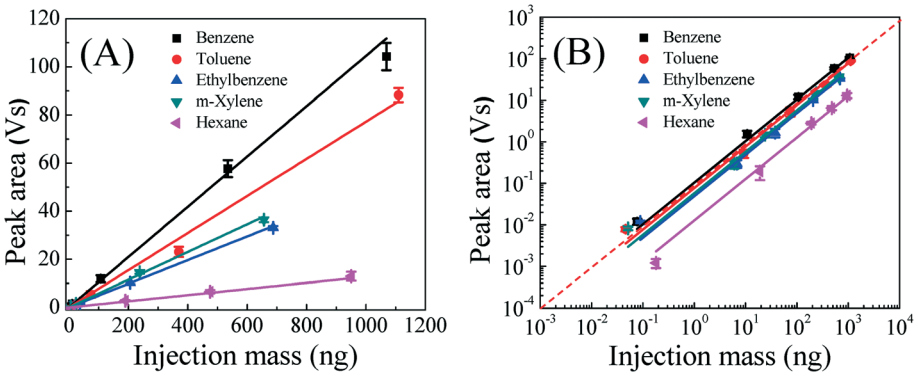

Fig. 5 Microfluidic PID linearity test for five different VOCs. (A) Peak area as a function of injection mass on the linear–linear scale. Solid lines are the linear fit (forced zero Y-intercept). The corresponding fit parameters are given in Table S2.† Error bars are obtained with 4 measurements. (B) The corresponding data and curves in (A) plotted on the log–log scale. The dashed line shows the curve with a unity slope to guide the eye.

GC separation

To demonstrate the performance of the microfluidic PID for a GC system, in Fig. 6, we separated nine VOC analytes using a 6 m long HP-5 column. The analytes were picked up at the headspace of the corresponding screw-thread vials and then injected into the injection port of a Varian 3800 GC instrument with a split ratio of 60. High purity helium and dry air were used as carrier gases at a flow rate of 2.0 mL min^{-1}. The column temperature was initially set at 40 °C for 0.2 minutes and then ramped to 75 °C at a rate of 30 °C min^{-1}. All the peaks were symmetric with peak widths (FWHM) below or around 1 s, which represents a drastic improvement over the previous GC separation results using the commercial PID and make-up gas.[37]

Conclusion and future work

We have developed a microfluidic PID that can be used in a GC (μGC) system for rapid and highly sensitive VOC detection. Due to its flow-through design and non-destructive nature, the microfluidic PID can be placed nearly anywhere in the flow path. Furthermore, the simple and robust structure as well as low voltage operation enables field applications of the microfluidic PID.

Future work will involve the tasks at the component level, sub-system level, and GC system level. At the component level, improvement will be implemented to further reduce the microfluidic PID base current and the relative noise to achieve an even better detection limit. For example, a UV shielding layer can be deposited to cover the exposed silicon. Different channel dimensions and serpentine structures will be explored to enhance the VUV illumination and ion collection efficiency. A compact electronic circuit will be built to replace the cumbersome amplifier and voltage supply. An electromagnetic shield will be constructed around the microfluidic PID to reduce electromagnetic interference. Furthermore, a micro-discharge based VUV light source that is micro-fabricated directly on the chip can also be explored to replace the VUV lamp.[33,34] At the sub-system level, a μGC separation column will be co-constructed on the same chip with the microfluidic PID to achieve higher integration. At the GC system level, the microfluidic PID will be installed in multi-dimensional μGC systems to monitor the analytes eluted from each dimension.[1] Finally, the microfluidic PID will be

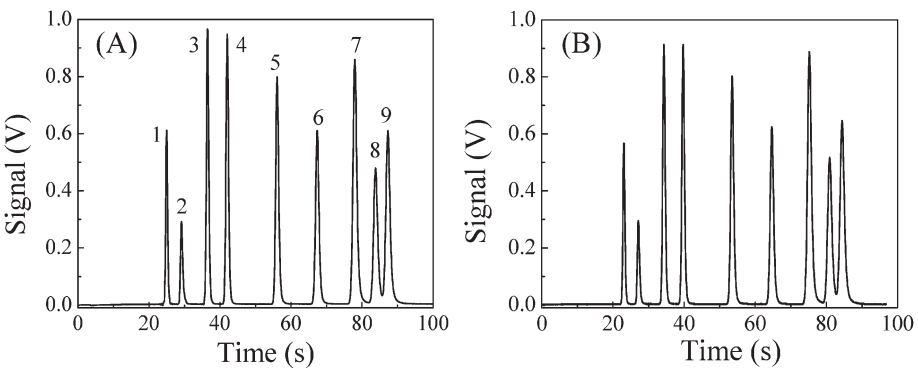

Fig. 6 Microfluidic PID detection of 9 VOCs separated by GC using a 6 m long HP-5 column. The injected masses and FWHMs were as follows: 1. vinyl chloride (2.1 ng, 0.6 s); 2. *cis*-1,2-dichloroethene (1.0 ng, 0.7 s); 3. benzene (1.2 ng, 0.7 s); 4. trichloroethylene (2.1 ng, 0.8 s); 5. toluene (1.5 ng, 0.9 s); 6. tetrachloroethylene (1.1 ng, 1 s); 7. chlorobenzene (1.0 ng, 1.2 s); 8. ethylbenzene (1.5 ng, 1.2 s); 9. *m*-xylene (1.5 ng, 1.3 s). Temperature ramping: T = 40 °C for 0.2 min and then to 75 °C at a rate of 30 °C min^{-1}. Helium (A) and dry air (B) were used as carrier gases at a flow rate of 2.0 mL min^{-1}.

used in tandem with other electronic vapor sensors such as graphene nanoelectronic vapor detectors[24] to achieve better discrimination in vapor sensing.

Acknowledgements

We would like to thank the National Science Foundation (IIP-1342917) and the Environmental Protection Agency (83564401) for financial support, and the Lurie Nanofabrication Facility for assistance in chip fabrication.

References

1 J. Liu, J. H. Seo, Y. Li, D. Chen, K. Kurabayashi and X. Fan, Smart multi-channel two-dimensional micro-gas chromatography for rapid workplace hazardous volatile organic compounds measurement, *Lab Chip*, 2013, **13**, 818–825.
2 K. B. Thurbide and T. C. Hayward, Improved micro-flame detection method for gas chromatography, *Anal. Chim. Acta*, 2004, **519**, 121–128.
3 C. H. Deng, X. H. Yang, N. Li, Y. Huang and X. M. Zhang, A novel miniaturized flame ionization detector for portable gas chromatography, *J. Chromatogr. Sci.*, 2005, **43**, 355–357.
4 J. W. Wang, H. Wang, C. F. Duan and Y. F. Guan, Micro-flame ionization detector with a novel structure for portable gas chromatograph, *Talanta*, 2010, **82**, 1022–1026.
5 W. Kuipers and J. Müller, Sensitivity of a planar micro-flame ionization detector, *Talanta*, 2010, **82**, 1674–1679.
6 J. Kim, B. Bae, J. Hammonds, T. Kang and M. A. Shannon, Development of a micro-flame ionization detector using a diffusion flame, *Sens. Actuators, B*, 2012, **168**, 111–117.
7 M. S. Klee, Detectors, in *Gas Chromatography*, ed. C. F. Poole, Elsevier, New York, 2012, ch 12.
8 S. Narayanan and M. Agah, Fabrication and Characterization of a Suspended TCD Integrated With a Gas Separation Column, *IEEE J. Microelectromech. Syst.*, 2013, **22**, 1166–1173.
9 Q. Y. Cai and E. T. Zellers, Dual-chemiresistor GC detector employing layer-protected metal nanocluster interfaces, *Anal. Chem.*, 2002, **74**, 3533–3539.
10 H. B. Lin and J. S. Shih, Fullerene C60-cryptand coated surface acoustic wave quartz crystal sensor for organic vapors, *Sens. Actuators, B*, 2003, **92**, 243–254.
11 P. R. Lewis, R. P. Manginell, D. R. Adkins, R. J. Kottenstette, D. R. Wheeler, S. S. Sokolowski, D. E. Trudell, J. E. Byrnes, M. Okandan, J. M. Bauer, R. G. Manley and G. C. Frye-Mason, Recent advancements in the gas-phase MicroChemLab, *IEEE Sens. J.*, 2006, **6**, 784–795.
12 D. L. McCorkle, R. J. Warmack, S. V. Patel, T. Mlsna, S. R. Hunter and T. L. Ferrell, Ethanol vapor detection in aqueous environments using micro-capacitors and dielectric polymers, *Sens. Actuators, B*, 2005, **107**, 892–903.
13 S. V. Patel, S. T. Hobson, S. Cemalovic and T. E. Mlsna, Detection of methyl salicylate using polymer-filled chemicapacitors, *Talanta*, 2008, **76**, 872–877.
14 L. K. Wright and E. T. Zellers, A nanoparticle-coated chemiresistor array as a microscale gas chromatograph detector for explosive marker compounds: flow rate and temperature effects, *Analyst*, 2013, **138**, 6860–6868.
15 S. I. Shopova, I. M. White, Y. Sun, H. Zhu, X. Fan, G. Frye-Mason, A. Thompson and S.-j. Ja, On-Column Micro Gas Chromatography Detection with Capillary-Based Optical Ring Resonators, *Anal. Chem.*, 2008, **80**, 2232–2238.
16 J. Liu, Y. Sun and X. Fan, Highly versatile fiber-based optical Fabry-Pérot gas sensor, *Opt. Express*, 2009, **17**, 2731–2738.
17 J. Liu, Y. Sun, D. J. Howard, G. Frye-Mason, A. K. Thompson, S.-J. Ja, S.-K. Wang, M. Bai, H. Taub, M. Almasri and X. Fan, Fabry-Perot Cavity Sensors for Multipoint On-Column Micro Gas Chromatography Detection, *Anal. Chem.*, 2010, **82**, 4370–4375.
18 Y. Sun, J. Liu, D. J. Howard, X. Fan, G. Frye-Mason, S.-j. Ja and A. K. Thompson, Rapid tandem-column micro-gas chromatography based on optofluidic ring resonators with multipoint on-column detection, *Analyst*, 2010, **135**, 165–171.
19 K. Reddy, Y. Guo, J. Liu, W. Lee, M. K. Khaing Oo and X. Fan, Rapid, sensitive, and multiplexed on-chip optical sensors for micro-gas chromatography, *Lab Chip*, 2012, **12**, 901–905.
20 K. Reddy, J. Liu, M. K. Khaing Oo and X. Fan, Integrated Separation Columns and Fabry-Perot Sensors for Microgas Chromatography Systems, *IEEE J. Microelectromech. Syst.*, 2013, **22**, 1174–1179.
21 K. Scholten, X. Fan and E. T. Zellers, Microfabricated optofluidic ring resonator structures, *Appl. Phys. Lett.*, 2011, **99**, 141108.
22 K. Scholten, X. Fan and E. T. Zellers, A microfabricated optofluidic ring resonator for sensitive, high-speed detection of volatile organic compounds, *Lab Chip*, 2014, **14**, 3873–3880.
23 C. Y. Lee, R. Sharma, A. D. Radadia, R. I. Masel and M. S. Strano, On-Chip Micro Gas Chromatograph Enabled by a Noncovalently Functionalized Single-Walled Carbon Nanotube Sensor Array, *Angew. Chem., Int. Ed.*, 2008, **47**, 5018–5021.
24 G. S. Kulkarni, K. Reddy, Z. Zhong and X. Fan, Graphene nanoelectronic heterodyne sensor for rapid and sensitive vapour detection, *Nat. Commun.*, 2014, **5**, 4376.
25 J. E. Lovelock, A sensitive detector for gas chromatography, *J. Chromatogr.*, 1958, **1**, 35–46.
26 J. G. W. Price, D. C. Fenimore, P. G. Simmonds and A. Zlatkis, Design and operation of a photoionization detector for gas chromatography, *Anal. Chem.*, 1968, **40**, 541–547.
27 N. Ostojić and Z. Šternberg, A new photoionization detector for gas chromatography, *Chromatographia*, 1974, **7**, 3–5.
28 A. N. Freedman, The photoionization detector: Theory, performance and application as a low-level monitor of oil vapour, *J. Chromatogr.*, 1980, **190**, 263–273.
29 P. Verner, Photoionization detection and its applications in gas chromatography, *J. Chromatogr.*, 1984, **300**, 249–264.
30 J. N. Driscoll and M. Duffy, Photoionization detector: A versatile tool for environmental analysis, *Chromatography*, 1987, **2**, 21–27.
31 S. J. Edwards, A. C. Lewis, S. J. Andrews, R. T. Lidster, J. F. Hamilton and C. N. Rhodes, A compact comprehensive two-dimensional gas chromatography (GCXGC) approach for

the analysis of biogenic VOCs, *Anal. Methods*, 2013, **5**, 141–150.

32 J. Sun, F. Guan, D. Cui, X. Chen, L. Zhang and J. Chen, An improved photoionization detector with a micro gas chromatography column for portable rapid gas chromatography system, *Sens. Actuators, B*, 2013, **188**, 513–518.

33 S. Narayanan, G. Rice and M. Agah, A micro-discharge photoionization detector for micro-gas chromatography, *Microchim. Acta*, 2014, **181**, 493–499.

34 M. Akbar, H. Shakeel and M. Agah, GC-on-Chip: Integrated Column and Photo Ionization Detector, *Lab Chip*, 2015, **15**, 1748–1758.

35 R. D. Cox and R. F. Earp, Determination of Trace Level Organics in Ambient Air by High-Resolution Gas Chromatography with Simultaneous Photoionization and Flame Ionization Detection, *Anal. Chem.*, 1982, **54**, 2265–2270.

36 A. T. Simpson, K. R. Hardwick, P. T. Walsh, R. C. Brown and M. A. Hemingway, Evaluation of diffusive samplers and photoionisation detectors for measuring very short peak exposures in the workplace, *J. Environ. Monit.*, 2003, **5**, 732–738.

37 R.-S. Jian, Y.-S. Huang, S.-L. Lai, L.-Y. Sung and C.-J. Lu, Compact instrumentation of a μ-GC for real time analysis of sub-ppb VOC mixtures, *Microchem. J.*, 2013, **108**, 161–167.

38 G. Lambertus, A. Elstro, K. Sensenig, J. Potkay, M. Agah, S. Scheuering, K. Wise, F. Dorman and R. Sacks, Design, Fabrication, and Evaluation of Microfabricated Columns for Gas Chromatography, *Anal. Chem.*, 2004, **76**, 2629–2637.

39 S. Reidy, G. Lambertus, J. Reece and R. Sacks, High-Performance, Static-Coated Silicon Microfabricated Columns for Gas Chromatography, *Anal. Chem.*, 2006, **78**, 2623–2630.

40 M. Liess and M. Leonhardt, New operation principle for ultra-stable photo-ionization detectors, *Meas. Sci. Technol.*, 2003, **14**, 427–432.

41 G. Baysinger, *CRC Handbook of Chemistry and Physics*, National Institute of Standards and Technology, 2014.